

[Click here to view linked References](#)

Evolution of microstructure and hardness during artificial aging of an ultrafine-grained Al-Zn-Mg-Zr alloy processed by high pressure torsion

Jenő Gubicza^{1,*}, Moustafa El-Tahawy², János L. Lábár^{1,3}, Elena V. Bobruk⁴, Maxim Yu Murashkin⁴, Ruslan Z. Valiev⁴ and Nguyen Q. Chinh¹

¹Department of Materials Physics, Eötvös Loránd University, Budapest, P.O.B. 32, H-1518, Hungary

²Department of Physics, Faculty of Science, Tanta University, 31527, Tanta, Egypt

³Institute for Technical Physics and Materials Science, Centre for Energy Research, Budapest, Hungary

⁴Institute of Physics of Advanced Materials, Ufa State Aviation Technical University, 12 K. Marx str., Ufa 450008 Russia

*Corresponding author: Tel: +36-1-372-2876, Fax: +36-1-372-2811,
e-mail: jeno.gubicza@ttk.elte.hu

E-mail addresses of the authors:

Moustafa El-Tahawy: mmt_eltahawy@yahoo.com

János L. Lábár: labar.janos@energia.mta.hu

Elena Bobruk: e-bobruk@yandex.ru

Maxim Yu Murashkin: m.murashkin.70@gmail.com

Ruslan Z. Valiev: ruslan.valiev@ugatu.su

Nguyen Q. Chinh: chinh@metal.elte.hu

Abstract

An ultrafine-grained (UFG) Al-4.8%Zn-1.2%Mg-0.14%Zr (wt.%) alloy was processed by high pressure torsion (HPT) technique and then aged at 120 and 170 °C for 2 h. The changes in the microstructure due to this artificial aging were studied by X-ray diffraction and transmission electron microscopy (TEM). It was found that the HPT-processed alloy has a small grain size of about 200 nm and a high dislocation density of about $8 \times 10^{14} \text{ m}^{-2}$. The majority of precipitates after HPT are Guinier-Preston (GP) zones with a size of ~2 nm and only a few large particles were formed at the grain boundaries. Annealing at 120 and 170 °C for 2 h resulted in the formation of stable MgZn₂ precipitates from a part of the GP zones. It was found that for the higher temperature the fraction of the MgZn₂ phase was larger and the dislocation density in the Al matrix was lower. The changes in the precipitates and the dislocation density due to aging were correlated to the hardness evolution. It was found that the majority of hardness reduction during aging was caused by the annihilation of dislocations and some grain growth at 170 °C. The aging effect on the microstructure and the hardness of the HPT-processed specimen was compared to that observed for the UFG sample processed by equal-channel angular pressing (ECAP). It was revealed that in the HPT sample less secondary phase particles formed in the grain boundaries, and the higher amount of precipitates in the grain interiors resulted in a higher hardness even after aging.

Keywords: Al-Zn-Mg-Zr alloy; high pressure torsion; aging; precipitates; dislocations; hardness

1. Introduction

Severe plastic deformation (SPD) is an effective and extensively studied way to produce ultrafine-grained (UFG) metals and alloys in the bulk form [1]. The two most frequently used

1 SPD methods are the equal-channel angular pressing (ECAP) and the high pressure torsion
2 (HPT) [2,3]. These techniques yield very hard materials due to the high dislocation density and
3
4 the small grain size developed during SPD [1, 4]. Additional hardening can be achieved by
5
6 post-SPD annealing due to segregation of solutes to lattice defects (e.g., to dislocations,
7
8 stacking faults and grain boundaries) [5-8], annihilation of mobile dislocations [9],
9
10 rearrangement of the remaining dislocations into harder configurations [10-12], clustering of
11
12 excess vacancies [13,14] and formation of precipitates [15-17]. The latter effect is very
13
14 important in age-hardenable materials, such Al-Zn-Mg alloys (7xxx series), where the
15
16 precipitate structure developed during SPD and subsequent annealing may differ from that
17
18 formed in coarse-grained counterparts during conventional aging heat treatments. It should
19
20 emphasized that due to their technological and practical importance, many features of AlZnMg
21
22 alloys have been studied in details [5,6,18-24]
23
24
25
26
27

28
29 In a recent publication, we investigated the microstructure-development and
30
31 mechanical properties of an ECAP-processed UFG Al-4.8%Zn-1.2%Mg-0.14%Zr (wt.%)
32
33 alloy aged at 120 and 170 °C up to the aging time of 2 h [25]. The evolution of hardness versus
34
35 the time of heat treatment can be seen in Figure 1a. Although, the hardness for the sample
36
37 processed by ECAP at room temperature (RT) was very high (~1470 MPa), after subsequent
38
39 aging at both 120 and 170 °C for 2 h the hardness decreased below the value characteristic to
40
41 the conventional T6 heat treatment (~1280 MPa). It was found that the hardness decrease was
42
43 mainly caused by the change of precipitates during annealing. Namely, η -MgZn₂ precipitates
44
45 formed from the GP zones and an additional particle coarsening also occurred. A large amount
46
47 of MgZn₂ precipitates were found in the grain boundaries after ECAP and the fraction and size
48
49 of these particles increased at the expense of the precipitates in the grain interiors. Thus, finally
50
51 the initially ECAP-processed sample became softer than the coarse-grained counterpart
52
53 subjected to the conventional T6 aging. The other very popular technique of SPD, the HPT
54
55
56
57
58
59
60
61
62
63
64
65

1 process was also applied on this alloy and the corresponding hardness evolution versus the
2 artificial aging time can be seen in Figure 1b. Although, the hardness of the HPT-processed
3 sample (~1970 MPa) was much higher than that for the ECAP specimen, the same aging
4 treatment caused similar or slightly lower softening in percentage (20-30%) as for the ECAP-
5 processed sample. At the same time, it is evident from Figure 1 that the hardness of the HPT-
6 processed specimen remained higher even after aging for 2 h than the value characteristic for
7 T6 conventional aging treatment. We aimed at investigating this difference by studying the
8 effect of aging on the microstructure of the HPT-processed alloy.
9

10
11
12
13
14
15
16
17
18
19 In this paper, the mentioned UFG Al-4.8%Zn-1.2%Mg-0.14%Zr (wt.%) alloy
20 processed by HPT at room temperature is aged artificially at 120 and 170 °C for 2 h. Then, the
21 change of the microstructure and the phase composition due to the heat treatments are studied
22 by X-ray diffraction (XRD) and transmission electron microscopy (TEM). In addition, the
23 hardness evolution during aging is investigated, and correlated to the changes in the dislocation
24 density and the precipitates. The thermal stability of the HPT-processed disk is compared with
25 the results obtained recently on an ECAP-processed alloy with the same composition [25]. It
26 is noted that the temperature and time of aging in this study were selected to agree with the
27 conditions often applied for the homogenization of the undeformed counterparts of Al-
28 4.8%Zn-1.2%Mg-0.14%Zr alloy [4, 25]. Therefore, the present results may be interesting not
29 only for basic research but also in practical applications.
30
31
32
33
34
35
36
37
38
39
40
41
42
43
44
45
46
47

48 **2. Materials and methods**

49 *2.1. Processing of the samples*

50
51 The alloy with the composition of Al-4.8%Zn-1.2%Mg-0.14%Zr (wt.%) was processed by
52 casting. The as-cast material was homogenized in air at 470 °C for 8 h, and then hot extruded
53 at 380 °C. Then, disks with a diameter of 20 mm and a thickness of 1.4 mm were cut from the
54
55
56
57
58
59
60
61

1 extruded rods for processing by HPT. Before HPT processing, the alloy was homogenized at
2 470 °C for 1 h and then water-quenched to RT. The disks were subjected to 10 turns of HPT at
3
4 RT under a pressure of 6 GPa and at a rotation speed of 1 rpm. The disks processed by HPT
5
6 were stored at RT for a long period (about 3 months) and then artificially aged at 120 °C or 170
7
8 °C for 2 h in an oil-bath. The effect of aging on the microstructure and hardness was studied at
9
10 the half-radius of the HPT-processed disk.
11
12
13
14
15
16

17 *2.2. Microstructure characterization techniques*

18
19
20 The phase composition and the microstructure of the HPT-processed and the aged specimens
21 were studied by X-ray diffraction (XRD). The diffraction patterns were taken by a rotating
22
23 anode diffractometer (type: MultiMax-9, manufacturer: Rigaku, Japan) using $\text{CuK}\alpha_1$ radiation
24
25 (wavelength: $\lambda = 0.15406$ nm). The diffraction domain size and the dislocation density in the
26
27 Al matrix were determined by X-ray line profile analysis (XLPA) of the diffraction patterns.
28
29 This analysis was performed by the Convolutional Multiple Whole Profile (CMWP) fitting
30
31 method [26]. In this procedure, the experimental diffraction pattern is fitted by the sum of a
32
33 background spline and the theoretical peak profiles calculated for each reflection. These
34
35 theoretical peaks were obtained as the convolution of the measured instrumental reflection and
36
37 the line profiles related to the diffraction domain size and the dislocations. The instrumental
38
39 pattern was measured on a LaB_6 line profile standard material. The area-weighted mean
40
41 diffraction domain size ($\langle x \rangle_{\text{area}}$) and the average dislocation density (ρ) were determined from
42
43 the line profile fitting. The area-weighted mean diffraction domain size was calculated as
44
45 $\langle x \rangle_{\text{area}} = m \cdot \exp(2.5 \sigma^2)$, where m is the median and σ^2 is the log-normal variance of the
46
47 diffraction domain size distribution.
48
49
50
51
52
53
54

55
56 The size and morphology of the matrix grains and the precipitates were characterized
57
58 by transmission electron microscopy (TEM). Thin TEM foils were prepared by mechanical
59
60
61
62
63
64
65

1 polishing in the first step and then thinned to perforation at -20 °C using a twin-jet
2 electropolishing unit with a chemical solution containing 33% HNO₃ and 67% CH₃OH.
3

4
5 A Titan Themis G2 200 scanning transmission electron microscope (STEM) was used
6
7 for TEM and energy-disperse X-ray spectroscopy (EDS) investigations. The microscope was
8
9 equipped with a four-segment Super-X EDS detector. A corrector for the spherical aberration
10
11 (C_s) was applied at the imaging part, while no probe-correction was present. The image
12
13 resolution is 0.16 nm in STEM Z-contrast imaging mode (recorded with a Fishione high-angle
14
15 annular dark-field (HAADF) detector). The EDS data were recorded (together with the HAADF
16
17 signal) in spectrum-image mode, and elemental maps were made for the constituents of the
18
19 alloy in order to study the size and morphology of the different precipitates. The grain size was
20
21 determined by measuring the diameters of the grains visible on the TEM images. About fifty
22
23 grains were evaluated for each sample and the average of the grain size was calculated. The
24
25 uncertainty of the grain size values was about 10%.
26
27
28
29
30
31

32 33 34 *2.3. Hardness testing*

35
36
37 A Zwick Roell ZH μ hardness tester was used for the measurement of the Vickers
38
39 microhardness of the samples. The experiments were performed at RT using an applied load
40
41 of 500 g and a dwell time of 10 s. The average hardness values were calculated from at least
42
43 10 individual measurements, with a relative error lower than 3%.
44
45
46
47
48

49 **3. Experimental results**

50 51 52 *3.1. XRD characterization of the phase composition and the microstructure of the HPT-* 53 54 *processed and the aged alloys*

55
56
57 Figure 2a shows the XRD diffraction pattern obtained for the HPT-processed sample. The
58
59 intensity is plotted in logarithmic scale in order to reveal whether small peaks of secondary
60
61

1 phases exist or not. It can be seen that only the diffraction peaks of the Al matrix appeared in
2 the pattern. Aging at 120 °C resulted in the development of a hexagonal η -MgZn₂ phase (PDF
3 card number: 34-0457) as revealed by the part of the diffraction pattern shown in Figure 2b.
4
5 Peaks of η' phase (PDF card number: 31-0024) were not observed by XRD. The fraction of
6
7 the η -MgZn₂ was characterized by the intensity ratio of this phase in the XRD pattern. This
8
9 quantity was determined as the ratio of the sum of the areas under the η -MgZn₂ peaks and the
10
11 sum of the areas under all peaks in the diffractogram in the diffraction angle range $2\theta = 30$ -
12
13 150° . Table 1 shows the data determined by using X-ray diffraction. It can be seen that the
14
15 XRD intensity fraction was $5.0 \pm 0.5 \%$ for the sample aged at 120 °C which increased to 8.3
16
17 $\pm 0.5 \%$ at 170 °C.
18
19
20
21
22

23
24 The average diffraction domain size and the dislocation density were determined by
25
26 XLP. As an example, Figure 3 shows the CMWP fitting on the diffraction pattern measured
27
28 for the HPT sample. The domain size and the dislocation density obtained for the HPT-
29
30 processed and the aged samples are also listed in Table 1. In the HPT specimen, the diffraction
31
32 domain size was 54 ± 6 nm while the dislocation density was $(8.0 \pm 0.9) \times 10^{14} \text{ m}^{-2}$. After aging
33
34 at 120 °C and 170 °C, the domain size increased to 73 ± 8 nm and 111 ± 12 nm, respectively.
35
36 The dislocation density decreased from $(8.0 \pm 0.9) \times 10^{14} \text{ m}^{-2}$ to $(2.6 \pm 0.3) \times 10^{14} \text{ m}^{-2}$ at 120
37
38 °C. During aging at 170 °C, the dislocation density decreased to a lower value of $(0.4 \pm 0.1) \times$
39
40 10^{14} m^{-2} .
41
42
43
44
45
46
47

48 3.2. TEM study of the microstructure

49

50
51 Figure 4 shows bright-field TEM images taken on the sample processed by HPT and the
52
53 specimens subsequently aged at 120 °C and 170 °C. The evaluation of numerous bright- and
54
55 dark-field TEM images yielded ~ 200 nm for the average grain size for the HPT-processed
56
57 alloy. It can also be seen that aging at 120 °C did not lead to significant grain coarsening while
58
59
60
61
62
63
64
65

1 at 170 °C the grain size increased to about 360 nm (see Table 2). It should be noted that the
2 grain size values determined by the present TEM study are larger with a factor of 3-4 than the
3 diffraction domain sizes obtained by XLPA (compare Tables 1 and 2). This difference has
4 already been observed for other SPD-processed samples and can be explained by the
5 hierarchical microstructure of the investigated materials [27]. Namely, X-ray diffraction is very
6 sensitive to small misorientations, therefore the domain size determined by XLPA reflects
7 rather the size of subgrains which is certainly lower than the grain size determined by TEM.
8

9
10
11
12
13
14
15
16
17 The evolution of precipitates during aging was studied using HAADF images and EDS
18 maps taken by the Titan Themis STEM. Figure 5a shows a HAADF image that reveals only
19 few precipitates in the grain boundaries (indicated by bright contrast as these precipitates must
20 contain elements heavier than Al, e.g., Zn and/or Zr). The HAADF image in Figure 5b shows
21 that there are precipitates not only in the boundaries but also in the grain interiors. The
22 corresponding EDS elemental maps for the main constituents (Al, Zn, Mg and Zr) are presented
23 in Figure 5c-f. These maps reveal that there are Mg/Zn-rich and Zr-rich precipitates in the
24 HPT-processed sample even if diffraction peaks of secondary phases did not appear in the XRD
25 patterns. This apparent contradiction can be explained by the very low concentration of Zr
26 which suggests only a low amount of Zr-rich precipitates. Most probably, these Zr-rich
27 precipitates are Al₃Zr particles as suggested by former studies (e.g., [28]). These Al₃Zr
28 precipitates pin effectively the grain boundaries, thereby resulting in a better thermal stability
29 of the UFG microstructure [29,30]. Therefore, the X-ray intensity scattered by these particles
30 was so weak that it can not be detected in the XRD pattern. Concerning the Mg/Zn-rich
31 precipitates, although they have a relatively large amount inside the grains as indicated by
32 HAADF and EDS images, their diffraction peaks also can not be detected in the XRD pattern
33 of the HPT sample. This observation suggests that the very small Mg/Zn-rich precipitates
34 (typical size: 2 nm) are Guinier-Preston (GP) zones which are enriched with Mg and Zn [19,20].
35
36
37
38
39
40
41
42
43
44
45
46
47
48
49
50
51
52
53
54
55
56
57
58
59
60
61
62
63
64
65

1
2
3
4
5
6
7
8
9
10
11
12
13
14
15
16
17
18
19
20
21
22
23
24
25
26
27
28
29
30
31
32
33
34
35
36
37
38
39
40
41
42
43
44
45
46
47
48
49
50
51
52
53
54
55
56
57
58
59
60
61
62
63
64
65

These GP zones are formed during HPT-processing and after storage of the samples at RT. From the evaluation of many HAADF images and EDS maps, the size of Mg/Zn-rich precipitates in the grain interiors ranged between 2 and 10 nm while in the grain boundaries their size varied between 10 and 20 nm. The average size of Mg/Zn-rich precipitates in the whole sample was ~10 nm (see Table 2). The diameter of the Zr-rich particles can be found in the range of 10-20 nm with an average value of 15 nm.

The HAADF images in Figure 6a and b show the precipitates in the HPT sample aged at 120 °C. The EDS maps corresponding to Figure 6b are presented in Figure 6c-f. In the grain interiors, the size of Mg/Zn-rich particles varied between 4 and 15 nm while in the grain boundaries their size was within the range of 20-60 nm. It can be concluded for both the Mg/Zn-rich and the Zr-rich precipitates that their average sizes increased to 25 and 20 nm, respectively, during aging at 120 °C (see Table 2). The change of average size of Zr-rich particles has recently been observed also in the alloy Al-0.4%Zr in the process of HPT. As was revealed in [31], such change was due to their dissolution during processing. For this aged sample, XRD peaks of the MgZn₂ phase appeared on the diffraction pattern, and the average domain size for this phase was determined from the breadth of the peak detected at the diffraction angle of about 40.4° (see Figure 2b). The obtained value (~25 nm) is in agreement with the average particle size obtained from the HAADF and EDS images (see Table 2). This result suggests that a significant amount of Mg/Zn-rich particles has η-MgZn₂ structure which is also supported by the relatively high fraction of η-MgZn₂ phase (~5%, see Table 1). Thus, it can be concluded that aging at 120 °C for 2 h resulted in a transition from GP zones to η-MgZn₂ precipitates.

Ageing at 170 °C resulted in further coarsening of the precipitates as shown in the HAADF images of Figures 7a and b. The EDS maps corresponding to Figure 7b are presented in Figures 7c-f. It is revealed that the average size of Mg/Zn-rich and Zr-rich particles increased

1
2
3
4
5
6
7
8
9
10
11
12
13
14
15
16
17
18
19
20
21
22
23
24
25
26
27
28
29
30
31
32
33
34
35
36
37
38
39
40
41
42
43
44
45
46
47
48
49
50
51
52
53
54
55
56
57
58
59
60
61
62
63
64
65

to ~40 and ~25 nm, respectively as shown in Table 2. Inside the grains, the size of precipitates is still lower (5-30 nm) than that in the grain boundaries (30-70 nm). The average diffraction domain size of the η -MgZn₂ phase (~45 nm) was close to the average size of the Mg/Zn-rich particles (~40 nm) determined from HAADF and EDS, suggesting that the majority of these precipitates has η -MgZn₂ structure, in accordance with the high fraction of this phase (~8.3%) in the diffraction pattern. It seems that the higher aging temperature yielded a more pronounced evolution of η -MgZn₂ phase from the GP zones and an additional precipitate coarsening.

3.3. Hardness of the HPT-processed and the aged specimens

The microhardness of the HPT-processed sample was 1970 ± 60 MPa. The hardness value decreased to 1620 ± 50 MPa and 1310 ± 30 MPa after aging at 120 °C and 170 °C, respectively. The reduction of hardness can be attributed to the decrease of the dislocation density and/or the changes in the precipitate structure during annealing as discussed in the next section.

4. Discussion

4.1. Correlation between the microstructure and the hardness

The obtained results provide evidence that HPT leads to significant microstructural changes in the alloy, where the formation of ultrafine grains is accompanied by the appearance of nanosized precipitates of secondary phases – Mg/Zn-rich and Zn-rich particles. These microstructural features markedly differ from those observed in conventional coarse-grained counterpart [25]. Moreover, recent observations on fine structure in HPT-processed Al alloys by means of precise atom probe tomography [32] made it possible to establish the formation of considerable segregations of Mg and Zn at grain boundaries, which may also have an effect on the mechanical properties, especially at high temperatures.

1
2
3
4
5
6
7
8
9
10
11
12
13
14
15
16
17
18
19
20
21
22
23
24
25
26
27
28
29
30
31
32
33
34
35
36
37
38
39
40
41
42
43
44
45
46
47
48
49
50
51
52
53
54
55
56
57
58
59
60
61
62
63
64
65

The decrease of the hardness due to aging can be attributed at least partly to the reduction of the dislocation density (see Table 1). The contribution of dislocation strengthening to the hardness (HV_{disl}) can be calculated from the Taylor-equation as:

$$HV_{disl} = 3\alpha M^T G b \rho^{1/2}. \quad (1)$$

The factor of three standing in the beginning of the right-hand side of this formula is used for taking the ratio of the hardness and the yield strength into account [33]. Moreover, in eq. (1) α describes the dislocation strengthening (about 0.32 for Al [34]), G is the shear modulus (~26 GPa for Al), b is the magnitude of the Burgers vector (~0.287 nm for Al) and M^T is the Taylor factor. Due to the lack of strong texture, M^T was taken as 3.06. The values of HV_{disl} calculated from the Taylor-equation for the HPT-processed sample and the aged specimens are listed in Table 3. Immediately after HPT, the hardness caused by the dislocation was 620 ± 60 MPa which is 31% of the total hardness value. Due to the reduction of the dislocation density during aging at 120 °C and 170 °C the value of HV_{disl} decreased to 350 ± 40 MPa and 140 ± 20 MPa, respectively. These values represent 21% and 11% of the total hardness for 120 °C and 170 °C, respectively, i.e., the contribution of dislocations to hardness decreased with increasing the aging temperature.

As was established in numerous works [1,32,35,36] the contribution of grain boundaries to the yield stress and ultimate tensile strength in the UFG materials processed by SPD techniques is quite considerable. According to the well-known Hall-Petch relationship, the strengthening contribution of the grain size can be written as:

$$HV_{GS} = K_H d^{-1/2}, \quad (2)$$

where d is the grain size and K_H is an appropriate constant associated with the hardness measurements. The value of K_H (210 MPa $\mu\text{m}^{1/2}$) was taken from [37], in which the Hall-Petch equation was investigated for a wide range of grain size in pure Al. The contribution of the grain size to the hardness for the HPT-processed and the aged specimens is shown in Table 3.

1 It can be seen that after HPT, the hardness, H_{GS} caused by the Hall-Petch effect was ~470 MPa
2 which is about 24% of the total hardness value. During aging at 120 °C, the value of H_{GS} did
3 not change, as the grain size remained unchanged, but for aging at 170 °C the value of H_{GS}
4 decreased to ~350 MPa, correspondingly to the grain-growth at this temperature.
5
6
7
8

9 The evolution of precipitates has also an impact on the change of the hardness during
10 aging. Although the total concentration of alloying elements did not change during aging, they
11 can appear in different forms in the matrix such as solute atoms, GP zones and η -MgZn₂
12 precipitates. It is well-known that the strengthening effects of these various structures may be
13 significantly different [19-21]. For instance, the increase in the size of GP zones at constant
14 volume fraction yields hardening since they can be cut by dislocations, while the coarsening
15 of η precipitates under similar conditions causes softening as they can not be cut by
16 dislocations. In the present study, the contribution of precipitates to hardness (HV_{precip}) was
17 calculated by subtracting the contributions of dislocations (HV_{disl}), grain size (HV_{GS}) and
18 lattice friction (HV_0) from the total measured hardness (HV_{total}):
19
20
21
22
23
24
25
26
27
28
29
30
31
32

$$33 \quad HV_{precip} = HV_{total} - (HV_0 + HV_{disl} + HV_{GS}). \quad (3)$$

34
35
36
37 Table 3 shows the values of HV_{precip} for the HPT-processed and the aged specimens. After
38 HPT, the hardness contribution of precipitates was 820 ± 130 MPa which were 740 ± 100 MPa
39 and 760 ± 60 MPa after aging at 120 °C and 170 °C, respectively. These data suggest that the
40 transformation of a part of GP zones to η -MgZn₂ particles during aging at 120 °C did not yield
41 significant reduction of hardness. This can be explained by the very moderate coarsening of
42 the precipitates in the grain interiors at 120 °C (from 2-10 nm to 4-15 nm), i.e., overaging did
43 not occur even if a considerable fraction of η phase was formed from the GP zones. In this
44 regard, only the precipitates inside the grains act as obstacles against dislocation glide,
45 therefore only their hardening effect should be considered here. The aging at 170 °C resulted
46 in also a practically unchanged contribution of precipitates to the hardness compared to the
47
48
49
50
51
52
53
54
55
56
57
58
59
60
61
62
63
64
65

1 HPT-processed sample (see Table 3). Although, the particles inside the grains were coarsened
2 from 4-15 nm to 5-30 nm when the aging temperature increased from 120 °C to 170 °C,
3
4 simultaneously the fraction of η -MgZn₂ phase increased from 5% to 8.3%. The latter effect
5
6 compensated partly the precipitate coarsening, therefore almost the same contribution of
7
8 precipitates to hardness was observed at 170 °C as compared to 120 °C.
9
10

11 12 13 14 *4.2. Comparison of aging effects in HPT- and ECAP-processed samples*

15
16 As it has been mentioned, in a recent publication [25] we investigated the aging
17
18 behavior of ECAP-processed Al alloy with the same composition. The ECAP was performed
19
20 through 4 passes using route B_C and the aging was carried out at the same temperature as for
21
22 the HPT specimen (120 °C and 170 °C). The dislocation density was lower ($\sim 4.8 \times 10^{14} \text{ m}^{-2}$)
23
24 than the value observed for the HPT disk ($\sim 8 \times 10^{14} \text{ m}^{-2}$). This difference can be explained by
25
26 the higher plastic strain and pressure used in HPT-processing. The high hydrostatic pressure
27
28 hinders diffusion [38-40] which is the basic mechanism of dynamic recovery, therefore the
29
30 dislocation density was higher for HPT compared to ECAP. At the same time, during aging the
31
32 decrease of the dislocation density was more pronounced for the HPT sample since the larger
33
34 initial dislocation density yields a higher driving force of recovery during annealing and the
35
36 diffusion is also faster at ambient pressure due to the higher amount of dislocations and grain
37
38 boundaries compared to the ECAP specimen. Thus, in the latter sample the dislocation density
39
40 decreased from $\sim 4.8 \times 10^{14} \text{ m}^{-2}$ only to $\sim 3.3 \times 10^{14} \text{ m}^{-2}$ at 170 °C while the aging for the HPT
41
42 disk yielded a much larger reduction in the dislocation density from $\sim 8 \times 10^{14} \text{ m}^{-2}$ only to ~ 0.4
43
44 $\times 10^{14} \text{ m}^{-2}$.
45
46
47
48
49
50
51
52

53 In the as-processed state, the ECAP sample contained η -MgZn₂ phase besides GP zones
54
55 while there were only GP zones in the HPT-processed specimen, i.e., the evolution of
56
57 precipitates was faster during ECAP-processing. This observation can also be explained by the
58
59
60
61
62
63
64
65

1 hindered diffusion during HPT due to the high applied pressure. This effect can impede the
2 development of stable η -MgZn₂ precipitates and only GP zones were observed after HPT.
3
4 When the HPT-processed sample was annealed at 120 °C and 170 °C, the high amount of grain
5 boundaries and dislocations yielded a higher diffusion rate, resulting in a fast development of
6
7 η -MgZn₂ precipitates. Indeed, the fraction of η phase for the HPT sample was much higher
8
9 than that for the ECAP specimen at both temperatures: for the ECAP samples 0.9% and 6.8%
10
11 were detected at 120 °C and 170 °C, respectively, while these values for the HPT disk were
12
13 5.0% and 8.3%.
14
15
16
17
18

19 Considering the dislocation densities and grain sizes obtained previously for ECAP-
20 processed samples [25], the contributions of different factors to hardness are recalculated by
21 using eqs. (2) and (3), and also listed in Table 3. It can be seen that the hardness of the HPT-
22 processed disk was much higher (~1970 MPa) than that for the ECAP specimen (~1470 MPa).
23
24 This difference can be explained by the higher dislocation density, lower grain size and the less
25 developed precipitates in the HPT disk. Namely, in the ECAP sample many large precipitates
26 (most probably η particles) can be found in the grain boundaries which developed due to the
27 accelerated diffusion along the grain boundaries during ECAP. However, these particles do not
28 contribute to hardening as they do not act as obstacles against the dislocation glide in the grain
29 interiors. As an example, the HAADF image in Figure 8a shows many particles in the grain
30 boundaries of the ECAP-processed specimen. At the same time, in the HPT specimen only a
31 very few particles can be found at the grain boundaries and the majority of precipitates are hard
32 GP zones (see Figure 5a). Therefore, the contribution of precipitates to the hardness (HV_{precip})
33 is much higher for the HPT sample (~820 MPa) than that for the ECAP specimen (~520 MPa).
34 This difference remained valid even after aging. Figure 8b and c show HAADF images for the
35 ECAP sample aged at 120 °C and 170 °C, respectively. Numerous coarse precipitates can be
36 seen in the grain boundaries which do not contribute to hardening. Therefore, the hardness
37
38
39
40
41
42
43
44
45
46
47
48
49
50
51
52
53
54
55
56
57
58
59
60
61
62
63
64
65

1 caused by the precipitates was much higher for the aged HPT samples than that for the ECAP-
2 processed and aged counterparts. Due to this effect, the total measured hardness values of the
3 aged HPT specimens were higher than that for the aged ECAP samples even if the dislocation
4 density was lower for the HPT disk at both 120 °C and 170 °C.
5
6
7
8

9 Table 3 reveals that for the HPT sample the hardness decreased by 350 MPa and 660
10 MPa after aging at 120 °C and 170 °C, respectively. For both temperatures, about the majority
11 (~75%) of this hardness reduction was caused by the annihilation of dislocations and only 25%
12 can be attributed to the change of grain size and precipitates (transformation from GP zones to
13 η phase and coarsening). At the same time, for the ECAP specimen the decrease of the hardness
14 during aging at 120 °C and 170 °C was only 240 MPa and 370 MPa, respectively, due to the
15 lower driving force for recovery, and the majority (higher than 80%) of the hardness decrease
16 was caused by the change of grain size and the precipitate structure. In the latter case, the coarse
17 η precipitates formed in the grain boundaries during ECAP were grown during aging at the
18 expense of the GP zones in the vicinity of boundaries which caused a pronounced softening.
19 In the HPT sample, less precipitates were not formed in the grain boundaries, and the softening
20 was caused mainly by the dislocation annihilation during aging due to the high driving force
21 of recovery.
22
23
24
25
26
27
28
29
30
31
32
33
34
35
36
37
38
39
40
41
42

43 **5. Conclusions**

44 The evolution of the microstructure and the hardness for a HPT-processed Al-Zn-Mg-Zr alloy
45 was studied during artificial aging at 120 and 170 °C. The following conclusions were drawn
46 from the experimental results:
47
48
49
50

- 51 1. An UFG microstructure with the grain size of ~ 200 nm and dislocation density of $\sim 8.0 \times$
52 10^{14} m^{-2} was formed during HPT. The majority of precipitates were GP zones with the size
53 of 2 nm which were located in the grain interiors. The average size of the Mg/Zn-rich and
54
55
56
57
58
59
60
61
62
63
64
65

1
2
3
4
5
6
7
8
9
10
11
12
13
14
15
16
17
18
19
20
21
22
23
24
25
26
27
28
29
30
31
32
33
34
35
36
37
38
39
40
41
42
43
44
45
46
47
48
49
50
51
52
53
54
55
56
57
58
59
60
61
62
63
64
65

Zr-rich precipitates were 10 and 15 nm, respectively. Peaks of η -MgZn₂ phase were not observed by XRD due to its very small fraction. It was found that the majority of the hardness was caused by the precipitates.

2. Aging at 120 and 170 °C, resulted in a significant decrease of the dislocation density to $\sim 2.6 \times 10^{14} \text{ m}^{-2}$ and $\sim 0.4 \times 10^{14} \text{ m}^{-2}$, respectively, due to the high driving force of recovery. In addition, a large amount of η -MgZn₂ particles was formed from the GP zones. The fractions of η -MgZn₂ phase were 5 and 8.3% at 120 and 170 °C, respectively. Moreover, coarsening of both Mg/Zn-rich and Zr-rich precipitates to 20-25 nm was also observed. These changes resulted in softening which was mainly caused by the decrease of the dislocation density.
3. The hardness of the HPT-processed sample (~ 1970 MPa) was much higher than that for the same alloy deformed by 4 passes of ECAP (~ 1470 MPa). This difference can be explained by the effect of the high pressure applied during HPT which hindered the diffusion necessary for the annihilation of dislocations and the formation of η -MgZn₂ precipitates from the GP zones. Thus, less large η -MgZn₂ particles were formed in the grain boundaries and more precipitates were found in the grain interiors in the HPT-processed sample which act as obstacles against dislocation motion. This difference between the ECAP and HPT specimens remained valid even after aging at 120 and 170 °C, resulting in a higher hardness for the HPT-processed sample even after annealing.

Acknowledgments

This research was supported by the Hungarian-Russian bilateral Research program (TÉT) No. 2017-2.3.4-TÉT-RU-2017-00005. This work was financed partly by the Ministry of Human Capacities of Hungary within the ELTE University Excellence program (1783-3/2018/FEKUTSRAT). This work was also supported by the project VEKOP-2.3.3-15-2016-

00002 of the European Structural and Investment Funds. RZV and MYM acknowledge the support in part from the Ministry of Science and Higher Education of the Russian Federation under grant agreement No. 14.586.21.0061 (unique project identifier RFMEFI58618X0061) and part from the Russian Foundation for Basic Research (project No. 20-03-00614).

Statement of conflicts of interest

The authors declare that there is no conflict of interest.

References

- [1] Valiev RZ, Zhilyaev AP, Langdon TG (2014) Bulk Nanostructured Materials - Fundamentals and Applications. John Wiley & Sons, Inc, Hoboken, New Jersey
- [2] Valiev RZ, Langdon TG (2006) Principles of equal channel angular pressing as a processing tool for grain refinement. *Prog Mater Sci* 51:881–981.
- [3] Zhilyaev AP, Langdon TG (2008) Using high-pressure torsion for metal processing: Fundamentals and applications. *Prog Mater Sci* 53:893–979.
- [4] Gubicza J (2017) Defect Structure and Properties of Nanomaterials. Woodhead Publishing, Duxford, UK
- [5] Liddicoat PV, Liao XZ, Zhao Y, Zhu Y, Murashkin MY, Lavernia EJ, Valiev RZ, Ringer SP (2010) Nanostructural hierarchy increases the strength of aluminium alloys. *Nat Commun* 1 (63):1-7.
- [6] Valiev RZ, Enikeev NA, Murashkin MY, Kazykhanov VU, Sauvage X (2010) On the origin of extremely high strength of ultrafine-grained Al alloys produced by severe plastic deformation. *Scr Mater* 63:949-952.
- [7] Zeng ZR, Zhu YM, Bian MZ, Xu SW, J. Davies CH, Birbilis N, Nie JF (2015) Annealing strengthening in a dilute Mg–Zn–Ca sheet alloy. *Scr Mater* 107:127–130.

- 1
2
3
4
5
6
7
8
9
10
11
12
13
14
15
16
17
18
19
20
21
22
23
24
25
26
27
28
29
30
31
32
33
34
35
36
37
38
39
40
41
42
43
44
45
46
47
48
49
50
51
52
53
54
55
56
57
58
59
60
61
62
63
64
65
- [8] Hu J, Shi YN, Sauvage X, Sha G, Lu K (2017) Grain boundary stability governs hardening and softening in extremely fine nanograined metals. *Science* 355:1292–1296.
- [9] Zeng W, Shen Y, Zhang N, Huang X, Wang J, Tang G, Shan A (2012) Rapid hardening induced by electric pulse annealing in nanostructured pure aluminum. *Scr Mater* 66:147–150.
- [10] Valiev RZ, Sergueeva A V, Mukherjee AK (2003) The effect of annealing on tensile deformation behavior of nanostructured SPD titanium. *Scr Mater* 49:669–674.
- [11] Gubicza J, Pereira PHR, Kapoor G, Huang Y, Subramanya Sarma V, Langdon TG (2018) Annealing-Induced Hardening in Ultrafine-Grained Ni–Mo Alloys. *Adv Eng Mater* 20:1800184.
- [12] Gubicza J (2020) Annealing-Induced Hardening in Ultrafine-Grained and Nanocrystalline Materials. *Adv Eng Mater* 22:1900507.
- [13] Su LH, Lu C, Tieu AK, He LZ, Zhang Y, Wexler D (2011) Vacancy-assisted hardening in nanostructured metals. *Mater Lett* 65:514–516.
- [14] Cengeri P, Kerber MB, Schafner E, Zehetbauer JM, Setman D (2019) Strengthening during heat treatment of HPT processed copper and nickel. *Mater Sci Eng A* 742:124–131.
- [15] Tian YZ, Freudenberger J, Pippan R, Zhang ZF (2013) Formation of nanostructure and abnormal annealing behavior of a Cu–Ag–Zr alloy processed by high-pressure torsion. *Mater Sci Eng A* 568:184–194.
- [16] Sun LX, Tao NR, Kuntz M, Yu JQ, Lu K (2014) Annealing-induced Hardening in a Nanostructured Low-carbon Steel Prepared by Using Dynamic Plastic Deformation. *J Mater Sci Technol* 30:731–735.

- 1
2
3
4
5
6
7
8
9
10
11
12
13
14
15
16
17
18
19
20
21
22
23
24
25
26
27
28
29
30
31
32
33
34
35
36
37
38
39
40
41
42
43
44
45
46
47
48
49
50
51
52
53
54
55
56
57
58
59
60
61
62
63
64
65
- [17] Darling KA, Kecskes LJ, Atwater M, Semones J, Scattergood RO, Koch CC (2013) Thermal stability of nanocrystalline nickel with yttrium additions. *J Mater Res* 28:1813–1819.
- [18] Mondolfo LF (1971) Structure of the Aluminium:Magnesium:Zinc alloys, *Int Metall Rev* 153:95-124.
- [19] Polmear IJ (1995) *Light Alloys-Metallurgy of the Light Metals*, 3rd ed. Arnold, London
- [20] Lendvai J (1996) Precipitation and Strengthening in Aluminium Alloys, *Mater Sci Forum* 217–222:43-56.
- [21] Chinh NQ, Lendvai J, Ping DH, Hono K (2004) The effect of Cu on mechanical and precipitation properties of Al-Zn-Mg alloys, *J Alloys Comp* 378:52-60.
- [22] Chinh NQ, Gubicza J, Czepe T, Lendvai J, Xu C, Valiev RZ, Langdon TG (2009) Developing a strategy for the processing of age-hardenable alloys by ECAP at room temperature, *Mater Sci Eng A* 516:248-252.
- [23] Chinh NQ, Györi T, Gubicza J, Lendvai J (2012) Possible self-organized criticality in the Portevin-Le Chatelier effect during decomposition of solid solution alloys, *MRS Communications* 2:1-4.
- [24] Valiev RZ, Kazykhanov VU, Mavlyutov AM, Yudakhina AA, Chinh NQ, Murashkin MY (2020) Superplasticity and High Strength in AlZnMgZrAlloy with Ultrfine Grains, *Adv Eng Mater* 22:1900555.
- [25] Gubicza J, Lábár JL, Lendvai J, Chinh NQ (2019) The influence of artificial aging on the microstructure and hardness of an Al–Zn–Mg–Zr alloy processed by equal-channel angular pressing. *J Mater Sci* 54:10918–10928.
- [26] Ribárik G, Gubicza J, Ungár T (2004) Correlation between strength and microstructure of ball-milled Al-Mg alloys determined by X-ray diffraction. *Mater Sci Eng A* 387–389:343–347.

- 1
2
3
4
5
6
7
8
9
10
11
12
13
14
15
16
17
18
19
20
21
22
23
24
25
26
27
28
29
30
31
32
33
34
35
36
37
38
39
40
41
42
43
44
45
46
47
48
49
50
51
52
53
54
55
56
57
58
59
60
61
62
63
64
65
- [27] Ungár T, Tichy G, Gubicza J, Hellmig RJ (2005) Correlation between subgrains and coherently scattering domains. *Powder Diffr* 20:366–375.
- [28] Priya P, Krane MJM, Johnson DR (2016) Precipitation of Al₃Zr Dispersoids During Homogenization of Al-Zn-Cu-Mg-Zr Alloys. *Light Met* 2016 211–218.
- [29] Eivani AR, Zhou J, Duszczyk J (2012) A new approach to incorporating the effect of nano-sized dispersoids on recrystallization inhibition into Monte Carlo simulation. *Comput Mater Sci* 54:370–377.
- [30] Buranova Y, Kulitskiy V, Peterlechner M, Mogucheva A, Kaibyshev R, Divinski SV, Wilde G (2017) Al₃(Sc,Zr)-based precipitates in Al–Mg alloy: Effect of severe deformation. *Acta Mater* 124:210–224.
- [31] Orlova TS, Mavlyutov AM, Latynina TA, Ubyivovk EV, Murashkin MY, Schneider R, Gerthsen D, Valiev RZ (2018) Influence of Severe Plastic Deformation on Microstructure, Strength and Electrical Conductivity of Aged Al–0.4Zr(Wt.%) Alloy. *Rev Adv Mater Sci* 55:92-101.
- [32] Zhang Y, Jin S, Trimby P, Liao X, Murashkin MY, Valiev RZ, Sha G (2019) Strengthening mechanisms in an ultrafine-grained Al-Zn-Mg-Cu alloy processed by high pressure torsion at different temperatures. *Mater Sci Eng A* 752:223-232
- [33] Tabor D (1951) *Hardness of Metals*, Clarendon Press, Oxford
- [34] Gubicza J, Chinh NQ, Lábár JL, Hegedűs Z, Xu C, Langdon TG (2008) Microstructure and yield strength of severely deformed silver. *Scr Mater* 58:775–778.
- [35] Furukawa M, Horita Z, Nemoto M, Valiev RZ, Langdon TG (1996) Microhardness measurements and the Hall-Petch relationship in an Al-Mg alloy with submicrometer grain size. *Acta Mater* 44:4619-4629.

- 1
2
3
4
5
6
7
8
9
10
11
12
13
14
15
16
17
18
19
20
21
22
23
24
25
26
27
28
29
30
31
32
33
34
35
36
37
38
39
40
41
42
43
44
45
46
47
48
49
50
51
52
53
54
55
56
57
58
59
60
61
62
63
64
65
- [36] Furukawa M, Iwahashi Y, Horita Z, Nemoto M, Tsenev NK, Valiev RZ, Langdon TG (1997) Structural evolution and the Hall-Petch relationship in an Al-Mg-Li-Zr alloy with ultrafine grain size. *Acta Mater* 45:4751-4757.
- [37] Farhat ZN, Ding Y, Northwood DO, Alpas AT (1996) Effect of grain size on friction and wear of nanocrystalline aluminum. *Mater Sci Eng A* 206:302–313.
- [38] Zehetbauer MJ, Stüwe HP, Vorhauer A, Schafner E, Kohout J (2003) The Role of Hydrostatic Pressure in Severe Plastic Deformation. *Adv Eng Mater* 5:330–337.
- [39] Schafner E (2010) Effects of releasing the hydrostatic pressure on the nanostructure after severe plastic deformation of Cu. *Scr Mater* 62:423–426.
- [40] Gubicza J, Dobatkin S V, Khosravi E, Kuznetsov AA, Labar JL (2011) Microstructural stability of Cu processed by different routes of severe plastic deformation. *Mater Sci Eng A* 528:1828–1832.

Figure and table captions

1
2
3
4 Fig. 1: Hardness as a function of ageing time at 120 and 170 °C for the samples processed by 4
5 passes of ECAP (a) and 10 turns of HPT (b). The blue ellipses indicate the studied states (aging
6
7 for 2 h).
8
9

10
11
12 Fig. 2: (a) XRD pattern for the HPT-processed sample in logarithmic intensity scale. (b) A part
13
14 of the XRD patterns in linear intensity scale measured on the HPT-processed sample and the
15
16 specimens aged at 120 and 170 °C for 2 h.
17
18

19
20 Fig. 3: The measured XRD pattern (open circles) and the diffractogram fitted by the CMWP
21
22 method (solid line) for the HPT-processed specimen. In order to a better visibility of the fitting
23
24 quality, the inset shows the magnified reflection 311 . The difference between the measured and
25
26 fitted data can be seen at the bottom of the inset.
27
28

29
30 Fig. 4: TEM images showing the microstructure for the HPT-processed sample (a) and the
31
32 specimens subsequently annealed at 120 (b) and 170 °C (c).
33
34

35
36 Fig. 5: (a,b) HAADF STEM images illustrating the microstructure of the HPT-processed
37
38 sample. (c-f) EDS elemental maps for Al, Zn, Mg and Zr obtained on the area shown in (b).
39
40

41
42 Fig. 6: (a,b) HAADF STEM images illustrating the microstructure of the specimen processed
43
44 by HPT and then aged at 120 °C for 2 h. (c-f) EDS elemental maps for Al, Zn, Mg and Zr
45
46 obtained on the area shown in (b).
47
48

49
50 Fig. 7: (a,b) HAADF STEM image illustrating the microstructure of the specimen processed by
51
52 HPT and then aged at 170 °C for 2 h. (c-f) EDS elemental maps for Al, Zn, Mg and Zr obtained
53
54 on the area shown in (b).
55
56

1
2
3
4
5
6
7
8
9
10
11
12
13
14
15
16
17
18
19
20
21
22
23
24
25
26
27
28
29
30
31
32
33
34
35
36
37
38
39
40
41
42
43
44
45
46
47
48
49
50
51
52
53
54
55
56
57
58
59
60
61
62
63
64
65

Fig. 8: TEM images showing the microstructure for the ECAP-processed sample (a) and the specimens subsequently annealed at 120 (b) and 170 °C (c).

Table 1: The XRD intensity fraction of η -MgZn₂ precipitates as well as the diffraction domain size and the dislocation density of the Al matrix as determined by XLPD.

Table 2: The average grain size in the Al matrix determined from TEM images and the average particle size of the Mg/Zn-rich and Zr-rich precipitates as obtained from the HAADF images and the EDS maps. The range of particle sizes for the precipitates is shown in the parentheses. The average diffraction domain size values for the MgZn₂ phase calculated from the XRD peak breadth are also listed.

Table 3: The total measured microhardness (HV_{total}), and the calculated contributions of the lattice friction (HV_0), dislocations (HV_{disl}), grain size (HV_{GS}) and precipitates (HV_{precip}). The total measured microhardness (HV_{total}), and the calculated contributions of the lattice friction (HV_0), dislocations (HV_{disl}), grain size (HV_{GS}) and precipitates (HV_{precip}). For the ECAP-processed and annealed samples, the hardness values were calculated from the microstructural parameters presented in Ref. [25].

Figure 1

[Click here to access/download;Figure;fig1.tif](#)

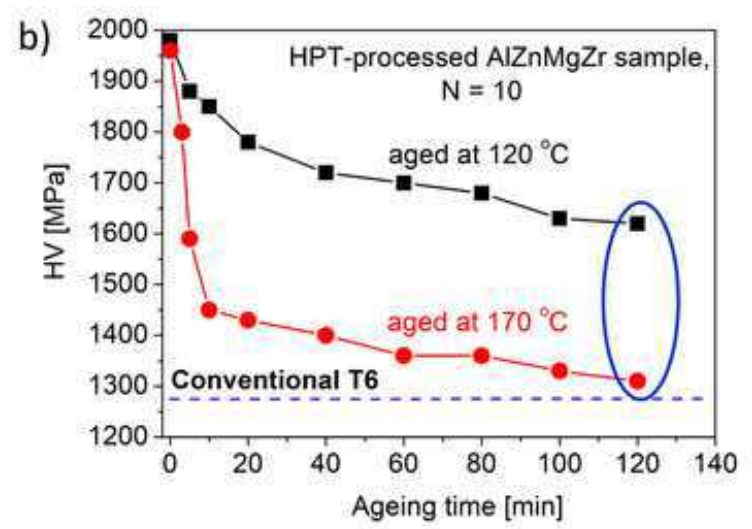
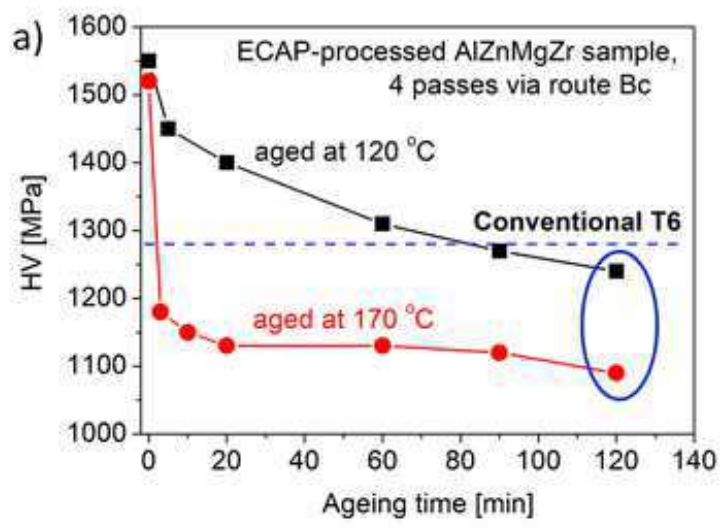


Figure 2

[Click here to access/download;Figure;fig2.tif](#)

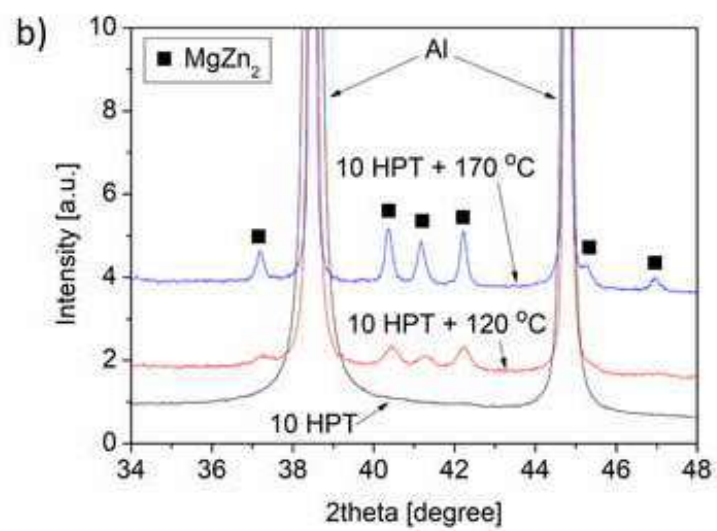
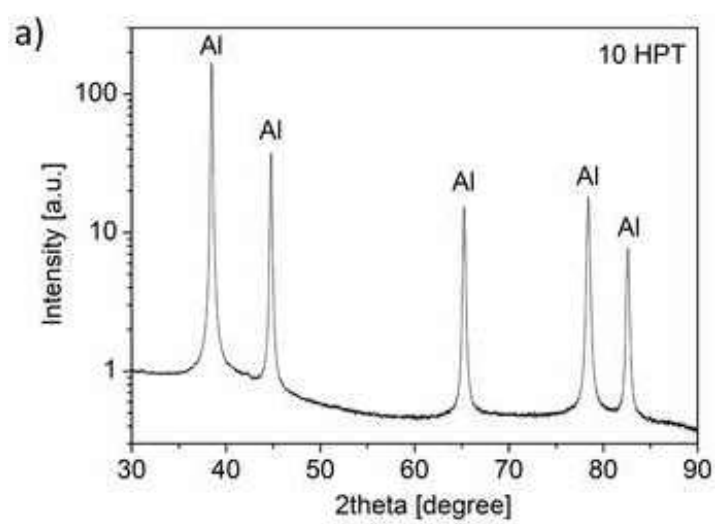


Figure 3

[Click here to access/download;Figure;fig3.tif](#)

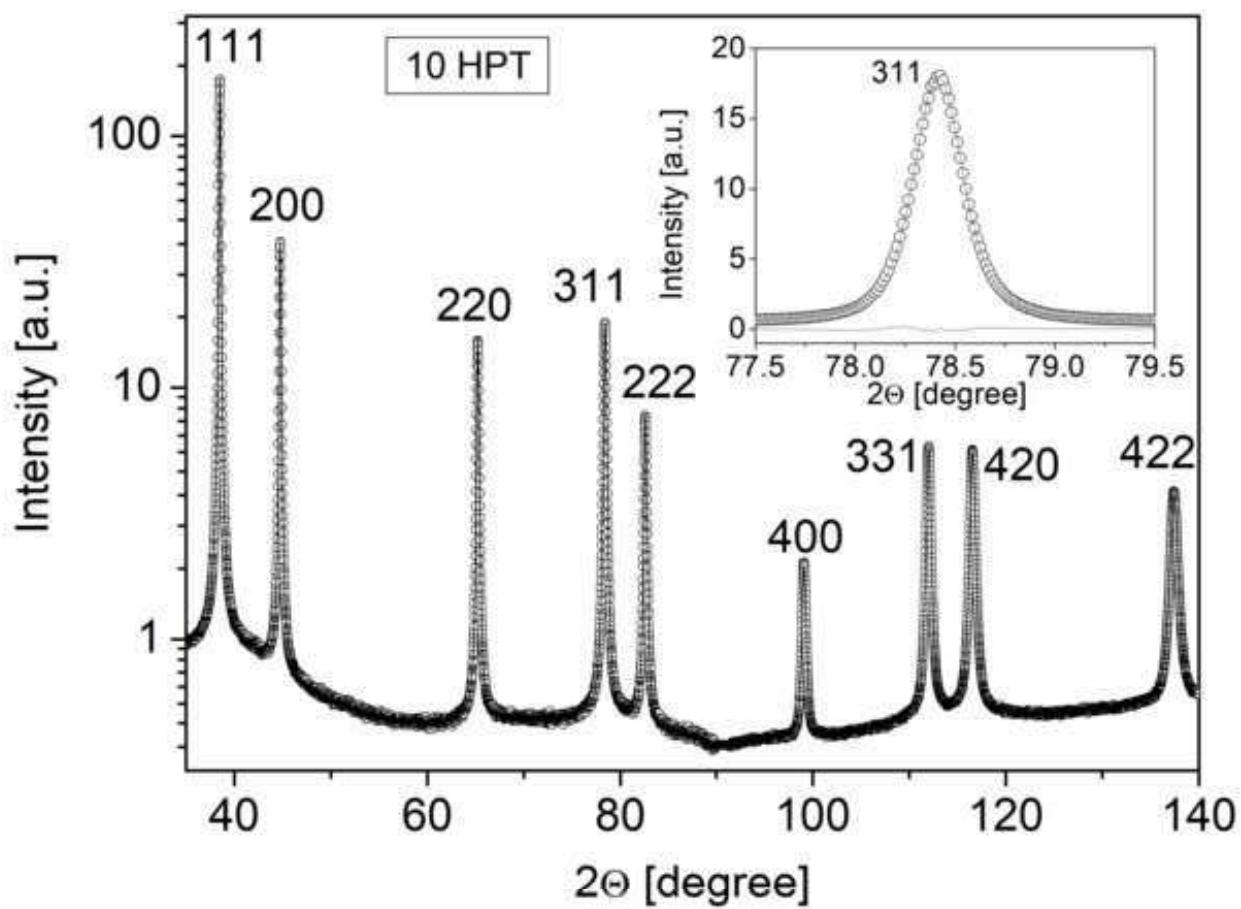


Figure 4

[Click here to access/download;Figure;fig4.tif](#)

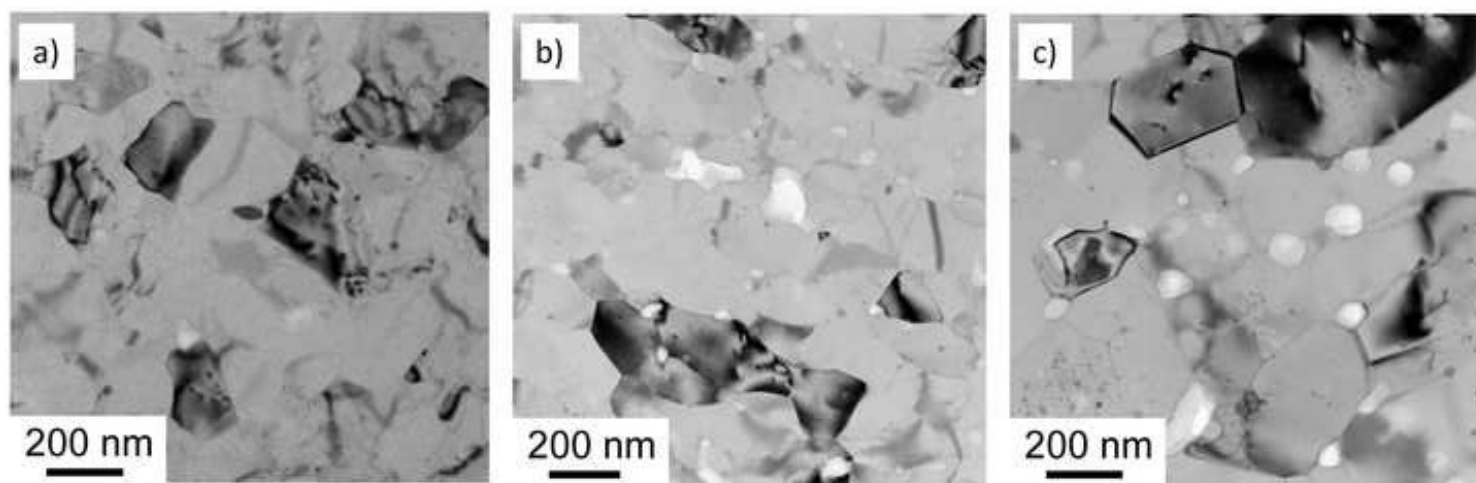


Figure 5

[Click here to access/download;Figure;fig5.tif](#)

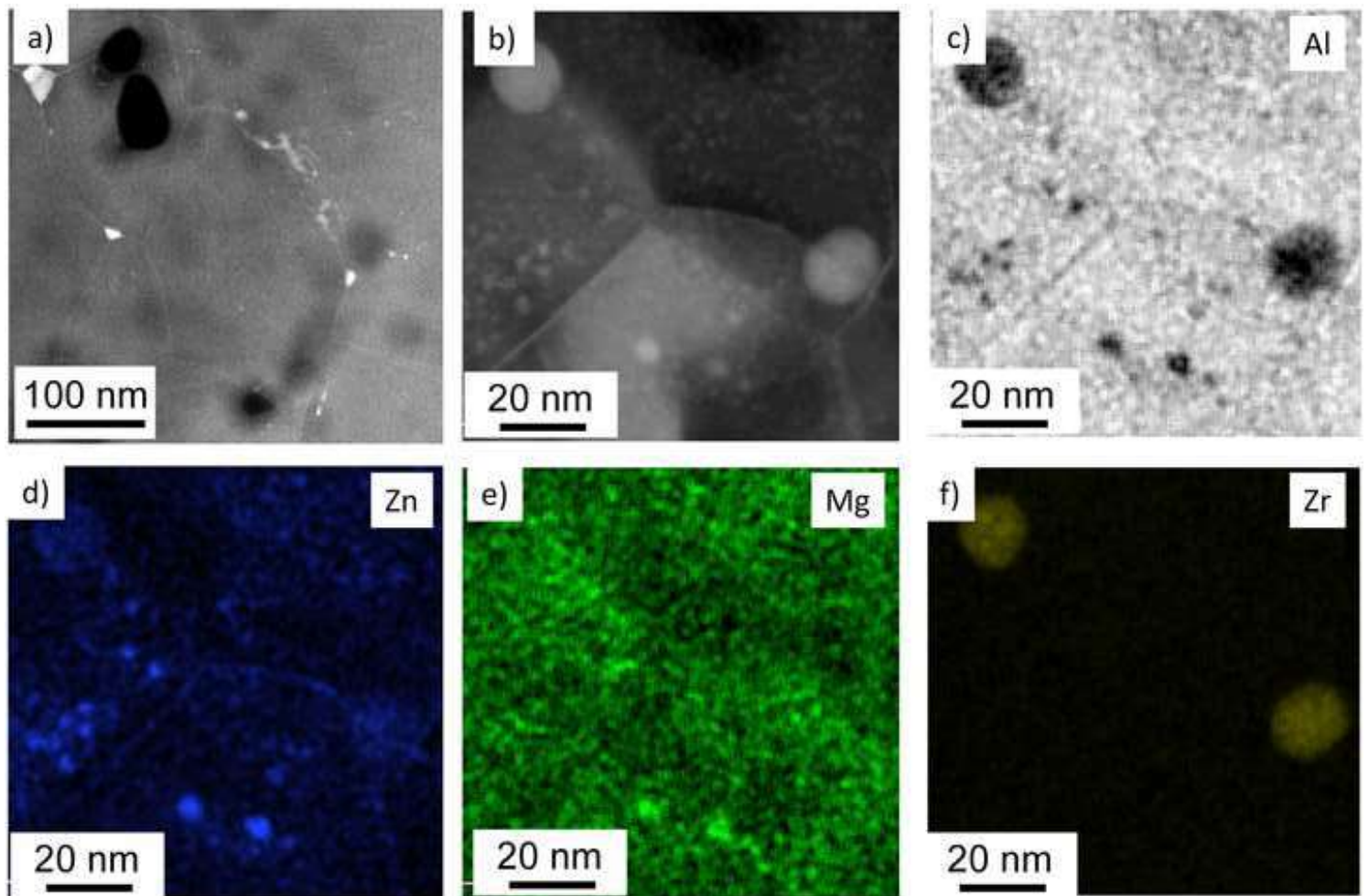


Figure 6

[Click here to access/download;Figure;fig6.tif](#)

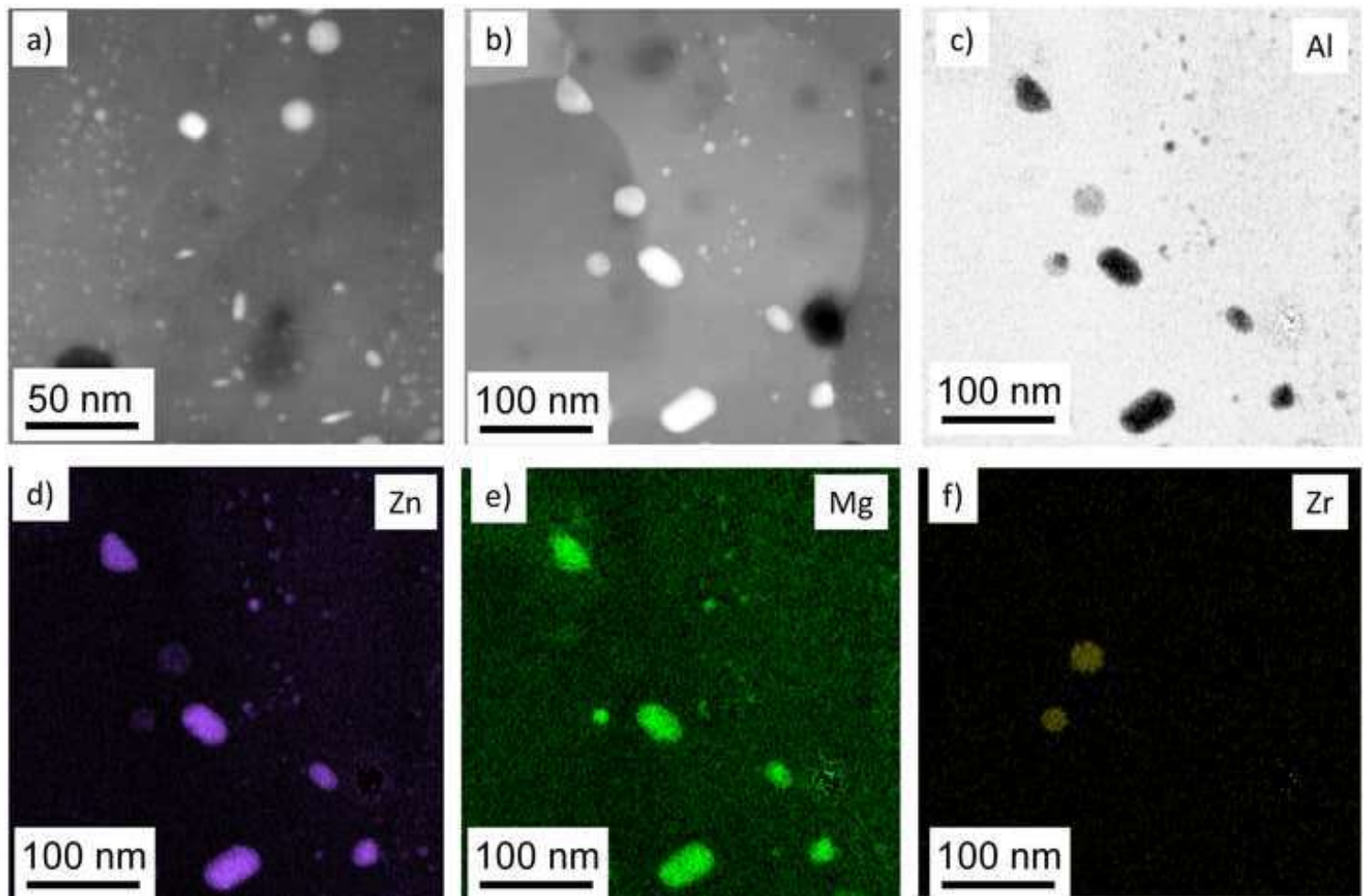


Figure 7

[Click here to access/download;Figure;fig7.tif](#)

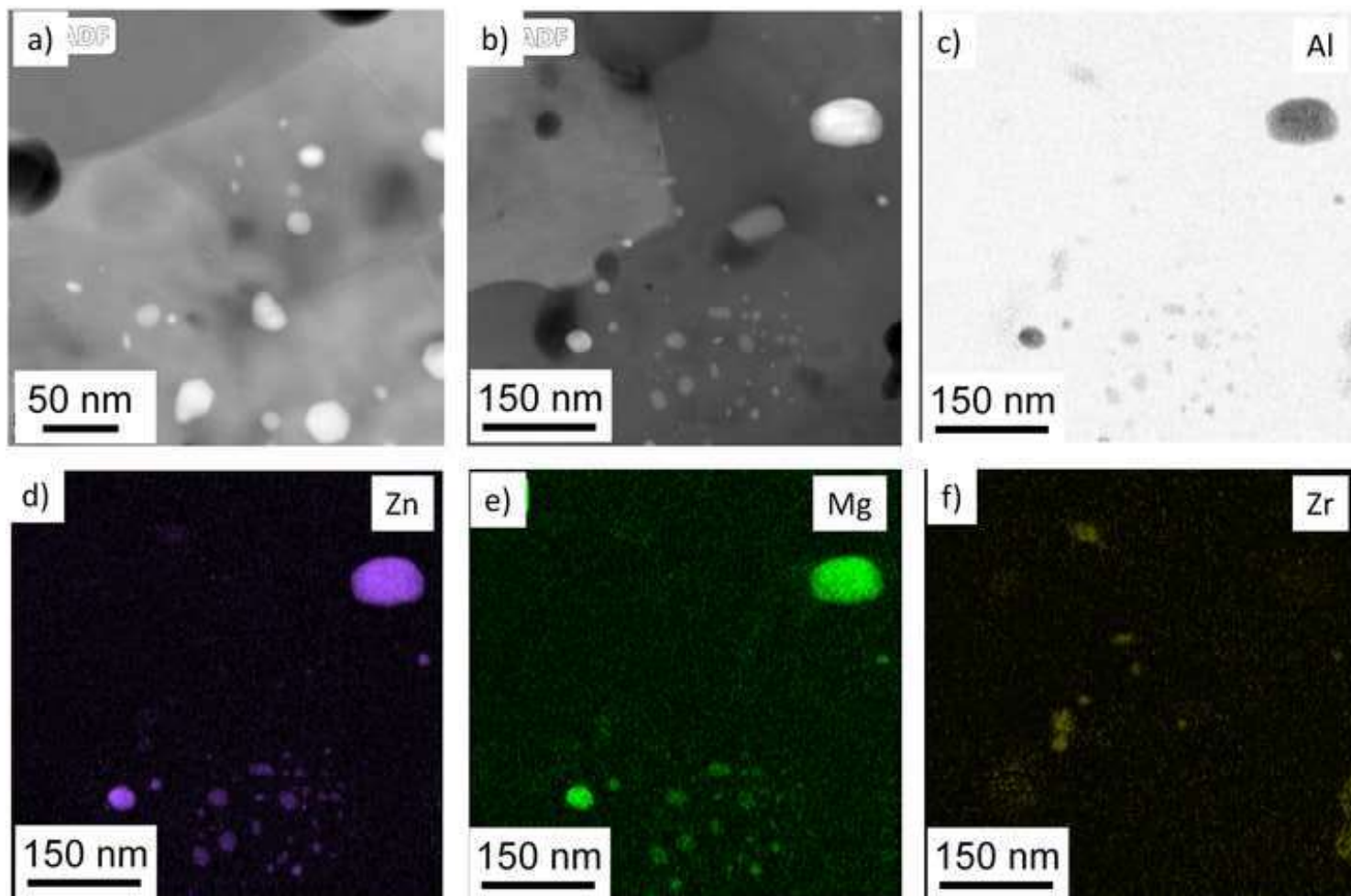


Figure 8

[Click here to access/download;Figure;fig8.tif](#)

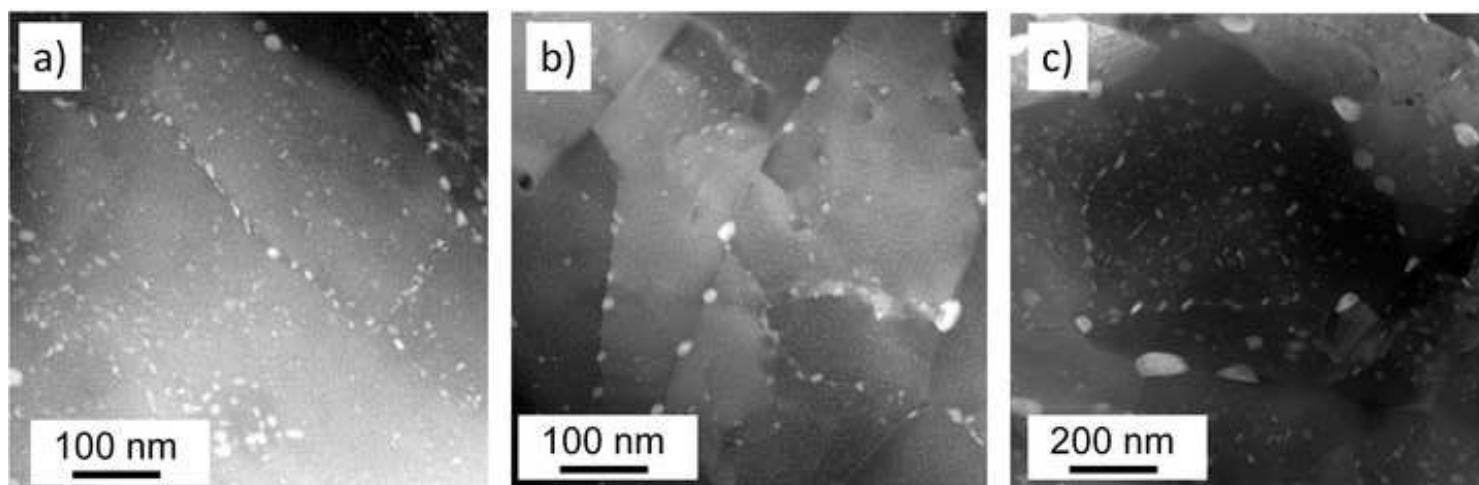


Table 1: The XRD intensity fraction of η -MgZn₂ precipitates as well as the diffraction domain size and the dislocation density of the Al matrix as determined by XLPAs.

Sample	Intensity fraction of MgZn ₂ [%]	Diffraction domain size in the matrix [nm]	Dislocation density in the matrix [10 ¹⁴ m ⁻²]
10 HPT at RT	0	54 ± 6	8.0 ± 0.9
10 HPT + aged at 120 °C	5.0 ± 0.5	73 ± 8	2.6 ± 0.3
10 HPT + aged at 170 °C	8.3 ± 0.5	111 ± 12	0.4 ± 0.1

Table 2: The average grain size in the Al matrix determined from TEM images and the average particle size of the Mg/Zn-rich and Zr-rich precipitates as obtained from the HAADF images and the EDS maps. The range of particle sizes for the precipitates is shown in the parantheses. The average diffraction domain size size values for the MgZn₂ phase calculated from the XRD peak breadth are also listed.

Sample	Grain size in the Al matrix [nm]	Particle size, Mg/Zn-rich [nm]	Particle size, Zr-rich [nm]	Diffraction domain size, MgZn ₂ [nm]
10HPT	200	10 (2-20)	15 (10-20)	-
10HPT + 120 °C	200	25 (4-60)	20 (10-30)	25
10HPT + 170 °C	360	40 (5-70)	25 (15-30)	45

Table 3: The total measured microhardness (HV_{total}), and the calculated contributions of the lattice friction (HV_0), dislocations (HV_{disl}), grain size (HV_{GS}) and precipitates (HV_{precip}). For the ECAP-processed and annealed samples, the hardness values were calculated from the microstructural parameters presented in Ref. [25].

Sample	HV_{total} [MPa]	HV_0 [MPa]	HV_{disl} [MPa]	HV_{GS} [MPa]	HV_{precip} [MPa]
10 HPT at RT	1970 ± 60	60 ± 10	620 ± 60	~ 470	820 ± 130
10 HPT + aged at 120 °C	1620 ± 50	60 ± 10	350 ± 40	~ 470	740 ± 100
10 HPT + aged at 170 °C	1310 ± 30	60 ± 10	140 ± 20	~ 350	760 ± 60
4 ECAP at RT	1470 ± 40	60 ± 10	480 ± 60	~ 410	520 ± 110
4 ECAP + aged at 120 °C	1230 ± 40	60 ± 10	480 ± 60	~ 380	310 ± 110
4 ECAP + aged at 170 °C	1100 ± 30	60 ± 10	400 ± 50	~ 290	350 ± 90